Journal of Materials Chemistry B

PAPER

Visualizing Mitochondria and Mouse Intestine with a Fluorescent Complex of a Naphthalene-based Dipolar Dye and Serum Albumin

Received 00th May 2020,
Accepted 00th June 2020

DOI: 10.1039/x0xx00000x

www.rsc.org/

Jong Min An,[a,‡] Heejo Moon,[b,‡] Yejin Kim,[c,d,‡] Sangrim Kang,[e] Youngseo Kim,[f] Yuna Jung,[a] Sungnam Park,[f] Peter Verwilst,[g,*] B. Moon Kim,[b,*] Jae Seung Kang,[c,d,*] and Dokyoung Kim,[a,e,h,i,*]

We have explored a new research field of fluorophores through the manipulation of fluorophore-binding proteins. The development of a new imaging agent for tracing a specific organelle or a particular site within a living organism has been of great interest in the field of basic science as well as translational medicine. In this work and for the first time, we will disclose a new naphthalene-based dipolar dye and its complex, with serum albumin (SA), and show their applicability for the selective imaging of mitochondria in cells and the intestine in a mouse. The SA-binding dipolar dye, IPNHC, was synthesized straightforwardly, and we identified its photophysical properties and binding mode with SA. IPNHC-SA complex showed a bright emission in the blue wavelength range with a high quantum yield and stability. In the fluorescence imaging study, bright fluorescence images of mouse intestines were observed under a UV light, as well as two-photon (TP) deep tissue imaging after intravenous injection of IPNHC and IPNHC-SA complex. The present findings hold great promise for the application of the fluorescent complex for use in the tracing and tracking of intestine-related diseases at clinical sites.

1. Introduction

Tracing a specific cellular organelle and site in the body is fundamentally crucial in the field of basic science and translational medicine.[1] There are various approaches for tracing involving novel materials, which are actively used in basic research and clinical settings.[2,3] Fluorescence-based approaches have made a significant contribution to tracking the dynamics of processes.[4,5] This involves following biological features in real-time, in vivo imaging at high-resolution, and the monitoring of specific sites of interest in an animal model as well as a human body with high selectivity.[6,7] They also have high biocompatibility and are relatively easy to operate in comparison to other methods, such as magnetic resonance imaging (MRI)[8] and positron emission tomography (PET).[9]

To date, various fluorescent materials have been introduced, including small organic fluorophores (dyes),[10,11] polymers,[12] and organic/inorganic nanomaterials.[13] These materials have been functionalized as bio-imaging agents and probes for fundamental biological study and practical applications, including metal ion sensing, disease biomarker analysis, and in vivo tissue imaging.[14-16] Recently, a complex formation approach between fluorophores and proteins has been spotlighted. BODIPY[17,18] and indocyanine green (ICG)[19] are also widely used fluorophores, which could be applied to cellular imaging, tissue imaging within animals, and image-guided surgery in a clinical setting.[20,21] However, an unexpected biological instability and the poor water solubility of these fluorophores have been pointed out as drawbacks,[22] and their low targeting ability requires additional chemical modification of their structure as well. To address these issues and maximize the applicability of the fluorophore, a complex formation approach with peptides or proteins was proposed.[23,24] The fluorescent quantum yield and stability of a fluorophore were significantly enhanced through the formation of a complex, and new biological and photophysical characteristics of the complex

[a] Department of Biomedical Science, Graduate School, Kyung Hee University, Seoul 02447, Republic of Korea
[b] Department of Chemistry, College of Natural Science, Seoul National University, Seoul 08826, Republic of Korea
[c] Laboratory of Vitamin C and Antioxidant Immunology, Department of Anatomy and Cell Biology, Seoul National University, College of Medicine, Seoul 03080, Republic of Korea
[d] Institute of Allergy and Clinical Immunology, Seoul National University Medical Research Center, Seoul 03080, Republic of Korea
[e] Department of Anatomy and Neurobiology, College of Medicine, Kyung Hee University, Seoul 02447, Republic of Korea
[f] Department of Chemistry, Korea University, Seoul 02841, Republic of Korea
[g] KU Leuven, Rega Institute of Medical Research, Medicinal Chemistry, 3000 Leuven, Belgium
[h] Center for Converging Humanities, Kyung Hee University, Seoul 02447, Republic of Korea
[i] Medical Research Center for Bioreaction to Reactive Oxygen Species and Biomedical Science Institute, School of Medicine, Graduate School, Kyung Hee University, Seoul 02447, Republic of Korea

† Electronic Supplementary Information (ESI) available. See DOI: 10.1039/x0xx00000x

‡ These authors contributed equally to this work.

* E-mail: dkim@khu.ac.kr (D.K.), genius29@snu.ac.kr (J.S.K.), kimbm@snu.ac.kr (B.M.K.), peter.verwilst@kuleuven.be (P.V.)

have been discovered, including an organ/disease site targeting ability, which was not present before the formation.[25-27]

Herein, we disclose a new fluorophore-protein complex based on a newly developed dipolar dye (named IPNHC) and serum albumin (SA), featuring unique properties; (i) bright blue emission with high fluorescence quantum yield (QY), (ii) high level of emission over a broad pH range, (iii) a mitochondria-targeted cellular imaging ability, and (iv) an intestine-targeted in vivo imaging ability within a healthy mouse. SA is a highly water-soluble albumin globular protein found in vertebrate blood and functions primarily as a carrier protein for steroids,[28] fatty acids,[29] and tyrosine-based thyroid hormones in the blood.[30,31] Because of the characteristics as a bio-carrier, SA has been widely used to enhance the biocompatibility of substrate (drug, dye, etc.) being utilized as an in vivo delivery system and a bio-imaging platform.[32] In this study, we attempted to discover entirely new photophysical and biological characteristics of the complex of SA and a newly exposed fluorophore, IPNHC. The synthesis and characterization of IPNHC were addressed in this article. This was prepared from the functionalized dipolar naphthalene platform (FDNP) (Fig. 1a),[33] and the biological properties of IPNHC and IPNHC-SA complex were demonstrated within the cell lines and healthy mice as a new fluorescent tracer. This study not only reports in-depth basic research but also shows the potential for practical applications throughout clinical research and translational medicine.

2. Results and discussion

Rationale

Recently, our research group has focused on the development of FDNP-based fluorophores and molecular probes to monitor the biologically important metal ions, disease biomarkers, cellular organelles, and disease-sites in animal models.[34,35] These naphthalene-based electron donor (D)-acceptor (A) type dipolar dyes have shown an array of advantages such as high biocompatibility, tunable manageable photophysical properties with the electron push/pull character change, and high two-photon absorbing abilities. Our key intermediate, DMHN1, has a dimethylamine (-NMe_2) group at the 6-position as a donor moiety, an aldehyde (-CHO) group at the 2-position as an acceptor moiety, and a hydroxy (-OH) group at the 3-position that can be used to introduce additional functional groups. Interestingly, DMHN1 is non-fluorescent due to excited-state intramolecular proton transfer (ESIPT), but emission can be recovered by blocking the ESIPT pathway (Fig. 1a).[36] During the study with DMHN1, we found a unique derivative using Mitsunobu reaction conditions. In 2005, Girard et al. firstly reported an unusual cascade reaction of hydrazone and carbonate formation within a single salicylaldehyde compound under the Mitsunobu reaction conditions using diisopropyl azodicarboxylate (DIAD) and triphenylphosphine (PPh_3) (Fig. 1b).[37] We introduced this chemistry to DMHN1 to prepare a hydrazone-containing fluorophore library with a suppressed ESIPT pathway. Along with this factor, we needed to increase the lipophilicity of the fluorophore to improve tissue uptake in animal studies.[38] In this aspect, the Mitsunobu reaction of DMHN1 was an efficient and straightforward approach to satisfy all our demands. The reaction product (named IPNHC) has a hydrazone moiety at the 2-position and carbonate moiety at the 3-position, accompanied by two isopropyl groups (*i*Pr) (Fig. 1c). Taking one step further, we introduced IPNHC to SA for the complex formation to find its new photophysical and biological properties.

Synthesis and photophysical property analyses of IPNHC

IPNHC was obtained from DMHN1 via an aza-Wittig reaction pathway under the standard Mitsunobu reaction conditions using DIAD and PPh_3 in tetrahydrofuran (THF) (yield: 71%) (Fig. 1c, Fig. S1, ESI†). The key intermediate DMHN1 was prepared from 2,7-dihydroxy-naphthalene in four synthetic steps, as previously reported by our group.[36] The purity of the synthesized IPNHC was verified by $^{1}H/^{13}C$ nuclear magnetic resonance (NMR) and high-resolution mass spectrometry (HRMS) (data in Electonic Supplementary Information; ESI†). The structure of IPNHC was further clearly identified through a single-crystal X-ray structure analysis (Fig. 1d, Table S3-S10, ESI†).

First, we studied the absorption and emission spectra of IPNHC in various solvents, as shown in Fig. 2a–2c and Table S1, ESI†. Generally, the naphthalene-based D-A type fluorophores, equipped with an imine functionality (-C=N-) or nitrile (-CN) at the electron acceptor (A) site and dialkylamine group (-NMe_2, -NEt_2, etc.) as the electron donor (D), show absorption and emission peaks in the blue region.[39] IPNHC was not an exception, showing peaks in the blue region (λ_{abs}=320–420 nm, λ_{emi}=400–600 nm) with a large Stokes shift and medium-dependent emission behavior that is a representative feature of D-A type dipolar fluorophores; (i) a hypsochromic emission peak shift as the solvent polarity decreases, (ii) a relatively lower emission intensity in protic polar solvents due to the decrement of intramolecular charge-transfer (ICT) and non-radiative decays in the excited state.[40] The emission intensity of IPNHC was strong in most organic solvents, including ethyl acetate (EtOAc, $\lambda_{emi\text{-}max}$=443 nm), dimethyl sulfoxide (DMSO, $\lambda_{emi\text{-}max}$=468 nm) and ethanol (EtOH, $\lambda_{emi\text{-}max}$=470 nm), and was weak in deionized water (DI H_2O, $\lambda_{emi\text{-}max}$=492 nm). One of the most important features was the large Stokes shift within most solvents (>100 nm, Table S1, ESI†). With fluorophores exhibiting small Stokes shifts, reabsorption of the emitted photons can cause a drop of signal to noise ratio (SNR) and fluorescence quantum yield (QY).[20,41] For IPNHC, the aggregation-induced photophysical property was not observed in aqueous media (deionized water), but it showed a strong correlation (R^2=0.977) between the emission intensity and the concentration of IPNHC (0–50 μM) with no peak shift (Fig. S2, ESI†).

Frontier orbitals (HOMO and LUMO) of an optimized structure of IPNHC were identified by a quantum chemical calculation (Fig. 2d, 2e). Each part of hydrazone and carbonate is located far apart, and the highest electron density was localized at the donor part (-NMe_2) in the HOMO and acceptor

part (hydrazone) in the LUMO. As a dipolar fluorophore, the electron density in the donor part could be transferred to the acceptor part, upon electronic excitation, as shown in frontier orbitals producing a charge transfer (CT) excited state. Thus, the UV-visible absorption and emission spectra of IPNHC exhibited significant solvatochromic properties in different solvents (Fig. 2a–2c). The calculated S_1 electronic emission spectrum ($\lambda_{emi\text{-}max}$=471 nm, in DMSO) corresponded with the experimental emission spectra (Fig. 2c), and a large oscillator strength (0.9) represented the efficient electronic transition from S_1 to S_0 state (Fig. 2f).

Photophysical properties of IPNHC-BSA

Our strategy was to take one step further and form the IPNHC-SA complex. In general, the ICT character of dipolar fluorophores could lead to the decrement of fluorescence QY within aqueous solvents, which makes the practical imaging applications challenging despite sufficient bright fluorescence images within cells and tissues. Through the formation of the IPNHC-SA complex, we expected an enhanced fluorescence QY and distinct biological properties suitable for bio-imaging.

The binding ability and photophysical property changes of IPNHC toward SA and various biomolecules were evaluated. Only bovine serum albumin (BSA), a representative SA, showed a significant emission intensity enhancement (Fig. 3a, 9-fold, at each maximum emission peak) with a hypsochromic shift of IPNHC (Fig. 3b, 3c, emission shift from 494 nm to 448 nm) in DI H_2O. Other species hardly gave changes despite the possibility of hydrazone/carbonate/carbamate hydrolysis. The emission enhancement was induced from two factors; (i) environmental changes of IPNHC to the relatively hydrophobic binding pocket of BSA, (ii) Förster resonance energy transfer (FRET) from tryptophan (Trp, λ_{emi}=300–450 nm)[42] within SA to IPNHC (λ_{abs}=300–440 nm). A significant emission decrement of BSA (at 350 nm) in the concentration-dependent titration study with IPNHC was observed (Fig. S3, ESI†). After confirming the selective complex formation of IPNHC and BSA with emission enhancement, the fluorescence QYs of IPNHC and IPNHC-BSA complex were measured in DI H_2O. The QY of IPNHC (Φ=0.1875) was dramatically enhanced (2.5-fold) after the complex formation with BSA (Φ=0.4677), as evidenced in comparison to the 9,10-diphenylanthracene (DPA) as a reference dye (Fig. S4, Table S2, ESI†).[43]

Furthermore, we confirmed the binding ability and photophysical properties of IPNHC toward SA derivatives, including BSA, fetal bovine serum (FBS), mouse serum (MS), goat serum (GS), and human serum (HS). The emission intensity of IPNHC was enhanced 11.5-fold in the presence of BSA, 16-fold with FBS, 7.18-fold with MS, 35.8-fold with GS, and 31.3-fold with HSA (Fig. S5, ESI†). These results represent that IPNHC could form a complex with most of the SA derivatives within the blood systems, both the animal SA (BSA, MS and GS) and human SA (HSA).

The effect of pH on the stability of the IPNHC-BSA complex was evaluated over a broad pH range, including physiological pH (pH 3–9, pH 7.4) (Fig. 3d, Fig. S6, ESI†). In the pH-dependent emission intensity analysis, the complex gave higher intensity in the pH range 7-9 than under acidic conditions. This is likely caused by a combination of the partial unfolding of BSA and an inefficient interaction of IPNHC within the pocket of BSA. High stability of the complex was observed at most of the pH levels up to 60 min, except basic pH levels (pH 8–9). Besides, a high photostability of the complex was observed under the intense light irradiation (365 nm, 3 W at focal plane) using a pH 5 buffer (Fig. S7, ESI†, >70% intensity over 60 min).

Binding mode analysis

The binding mode of IPNHC with BSA was investigated by molecular docking. Of the binding sites studied, the highest binding scores were observed at drug site 1, also known as the warfarin binding pocket or Sudlow's site 1 in the homologous HSA[44-46] and as the subdomain IIa of the protein. The best scoring model expresses an orientation to where the fluorophore core is bound to the lipophilic pocket, while more sterically hindered chains point to the pocket entrance. An analysis of the interaction in the proposed binding model between proteins and ligands revealed that the compound is predominately engaged in lipophilic interactions (Fig. 3e). The dimethylamine group makes close contact with Leu^{237}, Leu^{259}, Ala^{260}, Ile^{263}, and Ile^{289}, while the naphthalene core interacts with Leu^{237}, Ile^{289}, and Ala^{290}. The carbonate isopropyl group interacts with Ala^{290} as well, while the carbamate isopropyl group interacts with Val^{342} and Leu^{454}. Finally, the interaction was further stabilized by a hydrogen-bonding interaction between Arg^{198} and either one or both carbonyls of IPNHC (Fig. S8, ESI†).

The binding constant (K_b) of IPNHC to BSA was calculated using a linear fitting of the absorption titration curve, using a Benesi-Hildebrand relation[47,48] with warfarin, a well-known drug site inhibitor (Fig. S9, ESI†). IPNHC gave a K_b value of 1.02265×10^5 L*mol^{-1} for BSA, and the warfarin-containing set gave a slightly reduced value (0.76567×10^5 L*mol^{-1}). In the isothermal titration calorimetry (ITC) analysis, a value of 3.662×10^5 L*mol^{-1} (K_b) was derived for the complex of IPNHC and BSA within phosphate buffer (0.1 M, pH 7.2, 10% DMSO (*v/v*)) at 25 °C (Fig. S10, ESI†). From this data, we found that IPNHC prefers to bind to BSA binding site 1, which is a warfarin binding pocket (as the main binding site), and this observation lends support to the results of the docking experiment.

Cellular imaging

With these unique photophysical properties, IPNHC and IPNHC-BSA complex were applied to fluorescence cellular imaging (Fig. 4, Fig. S11, ESI†). To investigate the intracellular localization of IPNHC and IPNHC-BSA complex, IPNHC (20 μM) and IPNHC-BSA complex (20 μM IPNHC with 50 mg/mL BSA) were incubated for 60 min at 37 °C, and then commercial cellular organelle trackers (Mito-tracker; mitochondria, ER-tracker; endoplasmic reticulum, Lyso-tracker: lysosome) were post-incubated for 20 min within HeLa cell line (immortalized cervical cancer). Confocal laser scanning microscopy (CLSM) images showed a superior tracing

ability of IPNHC and IPNHC-BSA complex toward mitochondria (Pearson correlation coefficient; PPC, 0.90 for IPNHC, 0.95 for IPNHC-BSA complex) (Fig. 4) rather than other organelles (PCC 0.52 for ER, PCC 0.47 for lysosome) (Fig. S11, ESI†). The treatment of IPNHC could make a complex with albumin in the cell growth media due to FBS, and the in situ complex of IPNHC-albumin targeted mitochondria after cellular uptake. The fluorescence enhancement of IPNHC via in situ complex formation within the media was also confirmed in the in vitro analysis (Fig. S12, ESI†). After the IPNHC-BSA complex come into the cytosol, IPNHC could be released by the lysosomal BSA degradation pathway.[49-51] Free IPNHC could have a potential selectivity toward mitochondria due to the electrostatic interaction between the positively charged IPNHC and the negatively charged mitochondrial outer membrane (-160 mV).[52,53] The CCK-8 assay results revealed negligible cellular toxicity of IPNHC and IPNHC-BSA complex in a wide range of concentrations (0–100 μM IPNHC, 50 mg/mL BSA) (Fig. S13, ESI†). The viability of the HeLa cell maintains above 90% in the IPNHC-BSA complex, which indicated that IPNHC and IPNHC-BSA are applicable for further studies in basic science as well as translational research.

In vivo/Ex vivo tissue imaging

Given that IPNHC and IPNHC-BSA complex demonstrated promising biocompatibility and a targeted imaging ability to mitochondria in cells, we performed tissue imaging in live healthy mice (Fig. 5). In this study, we focused on the bio-distribution study aimed at finding the targeted imaging ability of IPNHC and IPNHC-BSA in animals (see the outline of the experimental process in Fig. 5a).

Firstly, we injected IPNHC and IPNHC-BSA complex into the tail vein of a healthy mouse (C57BL/6J). After 30 min circulation, an abdominal incision was conducted for the in vivo fluorescence signal monitoring of the internal organs. Interestingly, we observed bright blue fluorescence signals from the digestive system, such as duodenum (Du), jejunum (Je), and gallbladder (Ga) under UV-light irradiation (365 nm) for both IPNHC-only (group 2) and IPNHC-BSA sets (group 3) (Fig. 5b). Autofluorescence issues from the tissues in the given conditions did not appear (group 1, PBS-treated control).

For more accurate measurements, the mice were sacrificed, and the main organs were isolated (Fig. 5c). Under the same UV-light irradiation conditions mentioned above, the ex vivo imaging results from the dissected organs were consistent with the in vivo imaging results for both sets (IPNHC, IPNHC-BSA complex); bright fluorescence signals from the small intestine; Du (first section), Je (second section), and ileum (Il, final section). From these in vivo and ex vivo imaging results, we concluded that IPNHC-BSA could be homing the small intestine of live mice by making an in situ IPNHC-MSA complex within the mouse blood. We further analyzed the fluorescence images from the small intestine by separating the signals depending on the wavelength (Fig. 5d, 5e, Fig. S14, ESI†). A higher intensity distribution was observed at the blue emission channel (300-450 nm) for group 2 (purple) and group 3 (blue) rather than group 1 (black).

In view of these promising in vivo and ex vivo tissue imaging results, we conducted two-photon microscopy (TPM) imaging to identify the tissue permeability of the IPNHC-SA complex and its deep-tissue imaging ability. Prior to the TPM imaging, the two-photon absorption properties of IPNHC and IPNHC-BSA were confirmed using an established protocol. The two-photon action cross-section (TPACS, GM: Goeppert-Mayer unit) value of IPNHC-BSA was sizeable within a PBS buffer (pH 7.4) for TPM imaging; 50 GM at 730 nm, 66 GM at 740 nm, and 63 GM at 750 nm, and the values were slightly higher than that of acedan, a well-known two-photon absorbing fluorophore (Fig. 5f).[54-56] Although the TPACS values of IPNHC itself were low under the given condition; 54 GM at 730 nm, and 11 GM at 740 nm, 5 GM at 750 nm, it could be converted to IPNHC-SA complex in the biological system, which has high TPACS values. Besides, the TPACS values of IPNHC itself were sizeable in DMSO (Fig. S15, ESI†). After checking the TPACS values, we analyzed the fluorescence intensity and deep-tissue TPM images for the tissue samples depicted in Fig. 5c. High fluorescence intensity was observed only in the Je isolated from the IPNHC-BSA treated mouse (Fig. 5g, Fig. S16, ESI†). A depth-dependent TPM signal was recorded from the superficial layer to the internal layer (0–219 μm) for the intestine (jejunum), and the result represented a deep tissue imaging ability of IPNHC-BSA with high tissue permeability (Fig. 5h, Fig. S17, Fig. S18, ESI†). These TPM imaging results hold promise for applications of IPNHC-BSA complex to intestine-related diseases in clinical settings and can be used as a relatively simple and straightforward tool. We are currently performing various analytical experiments to find out the mechanisms of the in vivo homing characteristics of IPNHC-SA towards the intestine in live animals, and these results will be reported forthwith.

3. Conclusions

In this study, we disclosed a new fluorophore-protein complex that could be utilized to selectively visualize mitochondria and the mouse intestine for the first time. A new naphthalene-based dipolar dye (IPNHC) was synthesized by a cascade reaction of hydrazone formation and carbonate formation of the key intermediate (DMHN1) under the Mitsunobu reaction conditions, and its complex formation with serum albumin (IPNHC-SA) was fully characterized. IPNHC has a selective binding toward SA with significant fluorescence enhancement, and the resulting IPNHC-SA complex showed bright fluorescence at physiological pH levels with high stability. The photophysical properties of the IPNHC-SA complex were experimentally characterized and simulated using molecular docking analysis with a quantum chemical calculation as well. In the practical applications, IPNHC and IPNHC-SA complex treated with cell lines showed localized fluorescence images at mitochondria. Furthermore, we found that IPNHC and IPNHC-SA complex could distinguish the small intestine (duodenum, jejunum) of mice after injection in the tail vein and under the in vivo fluorescence imaging set-up, as well as ex vivo two-photon

microscopy. The in situ complex formation of IPNHC with SA in the cell growth media and mouse blood makes it possible to show the same functions for the IPNHC-SA complex. The lack of cytotoxicity supported the high biocompatibility of IPNHC and its SA complex. Based on our findings, we firmly believe that IPNHC and IPNHC-SA complex holds great promise for applications in basic research related to mitochondria and translational research pertaining to intestinal diseases.

4. Experimental

Synthesis of IPNHC

The synthetic procedure of IPNHC is summarized in Fig. S1 (ESI†). The preparation of the key intermediate, DMHN1, was performed according to the reported method.[36] For the synthesis of IPNHC, triphenylphosphine (PPh_3, 78 mg, 0.297 mmol) and diisopropyl azodicarboxylate (DIAD, 58 μL, 0.297 mmol) were added to a solution of DMHN1 (64 mg, 0.297 mmol) in anhydrous tetrahydrofuran (THF, 1.8 mL) at room temperature (25 °C). The resulted reaction mixture was then agitated overnight. The crude mixture was diluted with ethyl acetate (EtOAc) and washed with deionized water (DI H_2O) and brine. Subsequently, the organic layer was dried over magnesium sulfate ($MgSO_4$), filtered through a sintered glass filter, and concentrated under reduced pressure. The residue was purified by silica column chromatography (*n*-hexane/EtOAc = 3:1, *v*/*v*) to furnish IPNHC as a yellow solid (85 mg, 71%). ^{1}H NMR (400 MHz, $CDCl_3$): δ 1.32 (d, J = 4.0 Hz, 6H), 1.40 (d, J = 4.0 Hz, 6H), 3.05 (s, 6H), 5.00 (m, 1H), 5.09 (m, 1H), 6.80 (s, 1H), 7.11 (dd, J = 4.0, 8.0 Hz, 1H), 7,42 (s, 1H), 7.72 (d, J = 12.0, 1H), 8.03 (s, 1H), 8.07 (s, 1H), 8.32 (s, 1H); ^{13}C NMR (100 MHz, $CDCl_3$): δ 21.7, 22.1, 40.8, 69.5, 73.4, 105.9, 116.4, 117.2, 20.6, 124.7, 127.6, 129.7, 136.0, 139.6, 147.2, 149.0, 152.8. HRMS (*m/z*): $[M+Na]^+$ calcd. for $C_{21}H_{27}N_3NaO_5$, 424.1843; found, 424.1844.

UV/vis and fluorescence spectroscopic methods

UV/Vis absorption spectra were obtained using a spectrophotometer (Agilent Technologies Cary 8454, US). Fluorescence emission spectra were recorded on a spectro-fluorophotometer (SHIMADZU CORP. RF-6000, Japan). A stock solution of IPNHC was prepared in dimethyl sulfoxide (DMSO, 10 mM). The quartz cuvette (Hellma Analytics, Jena, Germany) for absorbance and fluorescence measurements has an internal volume of 100 μL or 1 mL. The photo-stability of IPNHC was analyzed under continuous UV light (365 nm, 3 W, Model RM104, Rayman, Rep. of Korea) in a pH 5 buffer for 60 min at 25 °C. During the light exposure, UV/Vis absorption spectra and emission spectra were monitored at a given time-lapse (5 min interval). Excitation at 350 nm was used. The biomolecules were screened using a spectro-fluorophotometer and were prepared in each vial after treated with IPNHC (final concentration: 10 μM). The spectra were recorded in deionized water (DI H_2O) or a buffer solution.

Docking mode analysis of IPNHC-BSA complex

The three-dimensional structure of IPNHC was generated using the MMFF94 force field[57] and used for the docking studies. A search box (30 × 30 × 30 Å) was placed at the center of the warfarin binding site (also known as drug site 1, located in subdomain IIA) of BSA crystal structures (PDB 3V03, 4F5S, 4JK4, 4OR0 and 6QS9),[58-62] with all ligands removed. Docking was performed using Autodock VINA[63] with exhaustiveness of 1000. The highest scoring binding positions were analyzed, and a shell of H_2O molecules was added using Ambertools as implemented in Chimera.[64] The hydrated structures were further refined using LigandScout 4.4.3.[65,66] The docked ligands, binding pocket side chains, and water surrounding the binding pocket were finally subject to a further MMFF94 force field energy minimization. Binding poses from this set of structures and the model with the best estimated binding affinity score from the remaining binding poses were selected as the model structure (any results where the MMFF94 optimized structure deviated significantly from the docked binding pose were discarded).

CLSM cellular imaging

Approximately 1×10^5 cells (HeLa) were seeded onto 35-mm glass confocal dishes and incubated for 24 h. At 80% confluency, the media was replaced with a serum-free media. 5 min later, cells were treated with IPNHC (10 μM) and IPNHC-BSA complex (10 μM IPNHC with 50 mg/mL of BSA) for 1 h at 37 °C in 5% CO_2 incubator. The cells were washed with PBS and treated with organelle tracker in a serum-free media for 20 min at 37 °C in 5% CO_2 incubator [Note: treatment volume and concentration of organelle tracker: 2 μL (1000× working concentration) of ER-Tracker Red, 1 μL of MitoTracker Deep Red FM (2000× working concentration), 1 μL of LysoTracker Deep Red (2000× working concentration)]. The cells were washed three times with PBS. After the washing, the cells were treated with 4% formaldehyde for 6 min, and the solution was then removed by washing it with PBS. The prepared samples were translated into images using confocal laser scanning microscopy (CLSM).

Ex vivo and in vivo imaging

Animal: C57BL/6J mice were kept in a specific pathogen-free condition at the animal facility of Seoul National University College of Medicine (Rep. of Korea). Six-to eight-week-old male mice weighing 20–25 g were used for the experiments. The animal protocol for the experiments was reviewed and approved by the Ethics Committee of Seoul National University. *Abdominal incision and in vivo/ex vivo imaging*: IPNHC (5 mg/kg) and IPNHC-BSA complex (5 mg/kg of IPNHC + 50 mg/mL of BSA, in PBS) were injected intravenously through the lateral tail vein. After injecting the mice, the circulation in mice spanned for 30 min. Afterward, the mice were anesthetized with Zoletil (25 mg/kg) and Rompun (10 mg/kg). To observe the organ distribution of IPNHC and IPNHC-BSA complex in mice with the naked eye, the middle abdominal region of the mouse was incised and monitored under a UV light lamp (365 nm, power: <1 W, Model RM104, Rayman, Rep. of Korea). For the ex vivo imaging, the organs were dissected with perfusion and then washed with PBS (3 times) in dark conditions. The resulting organs were monitored under the same conditions.
TPM imaging: After the ex vivo imaging, the mouse organs were fixed with 4% PFA for overnight. The organs were washed with

PBS (3 times) before the measurement with a two-photon microscope (TPM, Leica, Nussloch, Germany). The scanning two-photon microscopy equipped with a Titanium Sapphire laser (Chameleon vision, Coherent) and 25× water immersion objective lens was used for the ex vivo imaging of these tissue samples. The two-photon excitation wavelength was 750 nm using a laser power of approximately 50 mW at the focal plane, which provided the best image quality. Fluorescence intensity of the TPM images was analyzed using Leica software and Image-J software.

Conflicts of interest

The authors declare the following competing financial interest(s): The authors are listed as inventors on a pending patent application related to the technology described in this work.

Acknowledgments

This research was supported by National Research Foundation (NRF) of Korea (Ministry of Science and ICT, NRF-2019-M3A9H1103783). This research was also supported by Bio & Medical Technology Development Program of the NRF of Korea (Ministry of Science & ICT, NRF-2018-M3A9H3021707) and Basic Science Research Program through the NRF of Korea (Ministry of Education, NRF-2018-R1A6A1A03025124, NRF-2018-R1D1A1B07043383). Y.K. thanks the financial support from the NRF of Korea (NRF-2017-R1A6A3A11032576). B.M.K. thanks the financial support from the NRF of Korea (NRF-2012-M3A7B4049644). P.V. acknowledges support from Interne Fondsen KU Leuven/Internal Funds KU Leuven (STG/19/029).

Notes and references

1. A. R. Maity and D. Stepensky, *Molecular Pharmaceutics*, 2016, **13**, 1-7.
2. S. Louzoun-Zada, Q. Z. Jaber and M. Fridman, *Angewandte Chemie International Edition*, 2019, **58**, 15584-15594.
3. L. Rajendran, H.-J. Knölker and K. Simons, *Nature Reviews Drug Discovery*, 2010, **9**, 29-42.
4. A. Sharma, M.-G. Lee, M. Won, S. Koo, J. F. Arambula, J. L. Sessler, S.-G. Chi and J. S. Kim, *Journal of the American Chemical Society*, 2019, **141**, 15611-15618.
5. H. Zhu, J. Fan, J. Du and X. Peng, *Accounts of Chemical Research*, 2016, **49**, 2115-2126.
6. T. D. Ashton, K. A. Jolliffe and F. M. Pfeffer, *Chemical Society Reviews*, 2015, **44**, 4547-4595.
7. P. Gao, W. Pan, N. Li and B. Tang, *Chemical Science*, 2019, **10**, 6035-6071.
8. J. L. Fidler, L. Guimaraes and D. M. Einstein, *RadioGraphics*, 2009, **29**, 1811-1825.
9. C. G. Cronin, J. Scott, A. Kambadakone, O. A. Catalano, D. Sahani, M. A. Blake and S. Mcdermott, *The British Journal of Radiology*, 2012, **85**, 1211-1221.
10. X. Chen, F. Wang, J. Y. Hyun, T. Wei, J. Qiang, X. Ren, I. Shin and J. Yoon, *Chemical Society Reviews*, 2016, **45**, 2976-3016.
11. R. Zhang, G. Niu, X. Li, L. Guo, H. Zhang, R. Yang, Y. Chen, X. Yu and B. Z. Tang, *Chemical Science*, 2019, **10**, 1994-2000.
12. M. Abbas, Q. Zou, S. Li and X. Yan, *Advanced Materials*, 2017, **29**, 1605021.
13. T. Tang, Y. Wei, J. Kang, Z.-G. She, D. Kim, M. J. Sailor, E. Ruoslahti and H.-B. Pang, *Journal of Controlled Release*, 2019, **301**, 42-53.
14. M. D. Pluth, E. Tomat and S. J. Lippard, *Annual Review of Biochemistry*, 2011, **80**, 333-355.
15. J. J. A. Cotruvo, A. T. Aron, K. M. Ramos-Torres and C. J. Chang, *Chemical Society Reviews*, 2015, **44**, 4400-4414.
16. H. Li, G. Parigi, C. Luchinat and T. J. Meade, *Journal of the American Chemical Society*, 2019, **141**, 6224-6233.
17. N. Wang, Y. Wang, J. Gao, X. Ji, J. He, J. Zhang and W. Zhao, *Analyst*, 2018, **143**, 5728-5735.
18. S. Qi, N. Kwon, Y. Yim, V.-N. Nguyen and J. Yoon, *Chemical Science*, 2020, **11**, 6479-6484.
19. C. A. Davies-Venn, B. Angermiller, N. Wilganowski, P. Ghosh, B. R. Harvey, G. Wu, S. Kwon, M. B. Aldrich and E. M. Sevick-Muraca, *Molecular Imaging and Biology*, 2012, **14**, 301-314.
20. T.-B. Ren, W. Xu, W. Zhang, X.-X. Zhang, Z.-Y. Wang, Z. Xiang, L. Yuan and X.-B. Zhang, *Journal of the American Chemical Society*, 2018, **140**, 7716-7722.
21. V. A. Kuzmin, T. D. Nekipelova, T. A. Podrugina, G. V. Golovina, A. A. Kostyukov, V. V. Temnov, I. A. Doroshenko, E. V. Radchenko, V. A. Palyulin and N. S. Zefirov, *Photochemical & Photobiological Sciences*, 2016, **15**, 1377-1384.
22. M. Gao and B. Z. Tang, *ACS Sensors*, 2017, **2**, 1382-1399.
23. Y. Yao, L. Gui, B. Gao, Z. Yuan, Y. Chen, C. Wei, Q. He, F. Wang, M. Xu and H. Chen, *New Journal of Chemistry*, 2019, **43**, 1785-1790.
24. S. Lee, J. Xie and X. Chen, *Biochemistry*, 2010, **49**, 1364-1376.
25. W. Zhang, S. Song, H. Wang, Q. Wang, D. Li, S. Zheng, Z. Xu, H. Zhang, J. Wang and J. Sun, *Biomaterials*, 2019, **217**, 119279.
26. Q. Chen, C. Wang, Z. Zhan, W. He, Z. Cheng, Y. Li and Z. Liu, *Biomaterials*, 2014, **35**, 8206-8214.
27. F.-F. An and X.-H. Zhang, *Theranostics*, 2017, **7**, 3667-3689.
28. L. H. Geoffrey, *Journal of Endocrinology*, 2016, **230**, R13-R25.
29. G. J. van der Vusse, *Drug Metabolism and Pharmacokinetics*, 2009, **24**, 300-307.
30. R. Mahendhar, A. Shahbaz, M. Riaz, M. Aninyei, D. M. Reich and I. Sachmechi, *Cureus*, 2018, **10**, e2903-e2903.
31. S. Li, Y. Cao and F. Geng, *Evolutionary Bioinformatics*, 2017, **13**, 1176934317716089.
32. Z. Liu and X. Chen, *Chemical Society Reviews*, 2016, **45**, 1432-1456.
33. Y. Jung, N. K. Park, S. Kang, Y. Huh, J. Jung, J. K. Hur and D. Kim, *Analytica Chimica Acta*, 2020, **1095**, 154-161.
34. H. N. Kim, J. Lee, S. Park, J. Jung and D. Kim, *Sensors*, 2019, **19**, 2500.
35. Y. Jung, Y. Kim, N. H. Kim, J. Lee, K.-H. Kim, J. Jung, Y. Huh, H.-J. Jang, J. Joo, S. Park and D. Kim, *Dyes and Pigments*, 2019, **162**, 104-111.
36. I. Kim, D. Kim, S. Sambasivan and K. H. Ahn, *Asian Journal of Organic Chemistry*, 2012, **1**, 60-64.
37. M. Girard, P. Murphy and N. N. Tsou, *Tetrahedron Letters*, 2005, **46**, 2449-2452.

38. A. A. R. Mota, P. H. P. R. Carvalho, B. C. Guido, H. C. B. de Oliveira, T. A. Soares, J. R. Corrêa and B. A. D. Neto, *Chemical Science*, 2014, **5**, 3995-4003.
39. H. Moon, Y. Jung, Y. Kim, B. W. Kim, J. G. Choi, N. H. Kim, M. S. Oh, S. Park, B. M. Kim and D. Kim, *Organic Letters*, 2019, **21**, 3891-3894.
40. S. Singha, D. Kim, B. Roy, S. Sambasivan, H. Moon, A. S. Rao, J. Y. Kim, T. Joo, J. W. Park, Y. M. Rhee, T. Wang, K. H. Kim, Y. H. Shin, J. Jung and K. H. Ahn, *Chemical Science*, 2015, **6**, 4335-4342.
41. C. Yang, J. Zhang, W.-T. Peng, W. Sheng, D. Liu, P. S. Kuttipillai, M. Young, M. R. Donahue, B. G. Levine, B. Borhan and R. R. Lunt, *Scientific Reports*, 2018, **8**, 16359.
42. S. Paul, N. Sepay, S. Sarkar, P. Roy, S. Dasgupta, P. Saha Sardar and A. Majhi, *New Journal of Chemistry*, 2017, **41**, 15392-15404.
43. I. C. Sanchez and R. H. Lacombe, *The Journal of Physical Chemistry*, 1976, **80**, 2352-2362.
44. G. Sudlow, D. J. Birkett and D. N. Wade, *Molecular Pharmacology*, 1975, **11**, 824.
45. G. Sudlow, D. J. Birkett and D. N. Wade, *Molecular Pharmacology*, 1976, **12**, 1052.
46. J. Ghuman, P. A. Zunszain, I. Petitpas, A. A. Bhattacharya, M. Otagiri and S. Curry, *Journal of Molecular Biology*, 2005, **353**, 38-52.
47. D. Roy, A. Chakraborty and R. Ghosh, *RSC Advances*, 2017, **7**, 40563-40570.
48. M. Dong, T.-H. Ma, A.-J. Zhang, Y.-M. Dong, Y.-W. Wang and Y. Peng, *Dyes and Pigments*, 2010, **87**, 164-172.
49. M. J. Hawkins, P. Soon-Shiong and N. Desai, *Advanced Drug Delivery Reviews*, 2008, **60**, 876-885.
50. G. Zhu, G. M. Lynn, O. Jacobson, K. Chen, Y. Liu, H. Zhang, Y. Ma, F. Zhang, R. Tian, Q. Ni, S. Cheng, Z. Wang, N. Lu, B. C. Yung, Z. Wang, L. Lang, X. Fu, A. Jin, I. D. Weiss, H. Vishwasrao, G. Niu, H. Shroff, D. M. Klinman, R. A. Seder and X. Chen, *Nature Communications*, 2017, **8**, 1954.
51. R. Marwaha and M. Sharma, *Bio Protoc*, 2017, **7**, e2571.
52. J. Feher, in *Quantitative Human Physiology*, ed. J. Feher, Academic Press, Boston, 2012, DOI:10.1016/B978-0-12-382163-8.00021-9, pp. 180-190.
53. Y. Huang, X. You, L. Wang, G. Zhang, S. Gui, Y. Jin, R. Zhao and D. Zhang, *Angew Chem Int Ed Engl*, 2020, **59**, 10042-10051.
54. J. M. An, S. H. Kim and D. Kim, *Organic & Biomolecular Chemistry*, 2020, **18**, 4288-4297.
55. D. Kim, H. Moon, S. H. Baik, S. Singha, Y. W. Jun, T. Wang, K. H. Kim, B. S. Park, J. Jung, I. Mook-Jung and K. H. Ahn, *Journal of the American Chemical Society*, 2015, **137**, 6781-6789.
56. H. M. Kim and B. R. Cho, *Chemistry – An Asian Journal*, 2011, **6**, 58-69.
57. M. Falk, P. F. Spierenburg and J. A. Walter, *Journal of Computational Chemistry*, 1996, **17**, 409-417.
58. K. A. Majorek, P. J. Porebski, A. Dayal, M. D. Zimmerman, K. Jablonska, A. J. Stewart, M. Chruszcz and W. Minor, *Molecular Immunology*, 2012, **52**, 174-182.
59. A. Bujacz, *Acta Crystallographica Section D*, 2012, **68**, 1278-1289.
60. B. Sekula, K. Zielinski and A. Bujacz, *International Journal of Biological Macromolecules*, 2013, **60**, 316-324.
61. A. Bujacz, K. Zielinski and B. Sekula, *Proteins: Structure, Function, and Bioinformatics*, 2014, **82**, 2199-2208.
62. R. Castagna, S. Donini, P. Colnago, A. Serafini, E. Parisini and C. Bertarelli, *ACS Omega*, 2019, **4**, 13270-13278.
63. O. Trott and A. J. Olson, *Journal of Computational Chemistry*, 2010, **31**, 455-461.
64. E. F. Pettersen, T. D. Goddard, C. C. Huang, G. S. Couch, D. M. Greenblatt, E. C. Meng and T. E. Ferrin, *Journal of Computational Chemistry*, 2004, **25**, 1605-1612.
65. G. Wolber and T. Langer, *Journal of Chemical Information and Modeling*, 2005, **45**, 160-169.
66. G. Wolber, A. A. Dornhofer and T. Langer, *Journal of Computer-Aided Molecular Design*, 2006, **20**, 773-788.

Figures

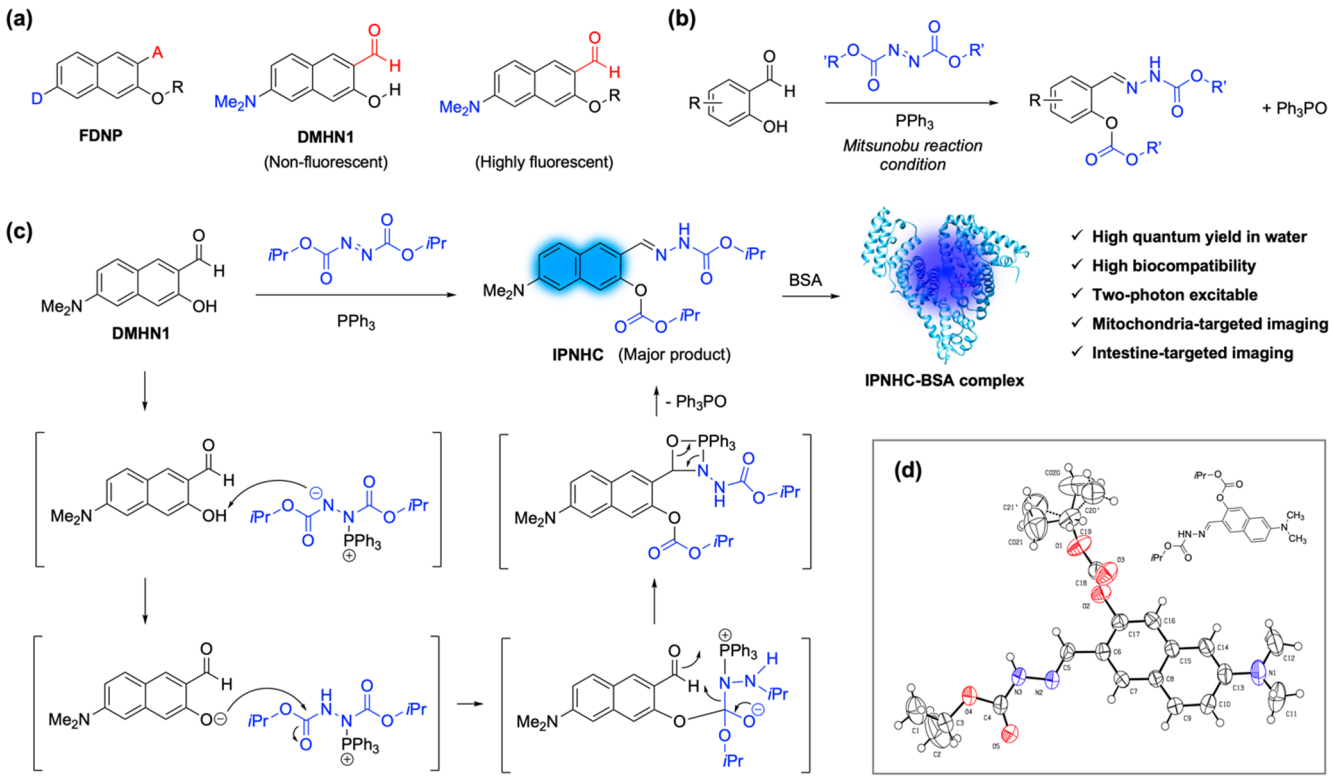

Fig. 1. Synthesis of IPNHC and its BSA complex formation. (a) Chemical structure of FDNP and DMHN1. (b) The formation of a hydrazone from salicylaldehydes under normal Mitsunobu reaction conditions in the presence of triphenylphosphine (PPh_3) and diisopropyl azodicarboxylate (DIAD). (c) Synthesis of IPNHC from DMHN1 under Mitsunobu reaction conditions, and its complex formation with BSA. The merits of IPNHC-BSA are outlined. (d) Crystal structure of IPNHC where oxygen and nitrogen atoms are represented in red and blue.

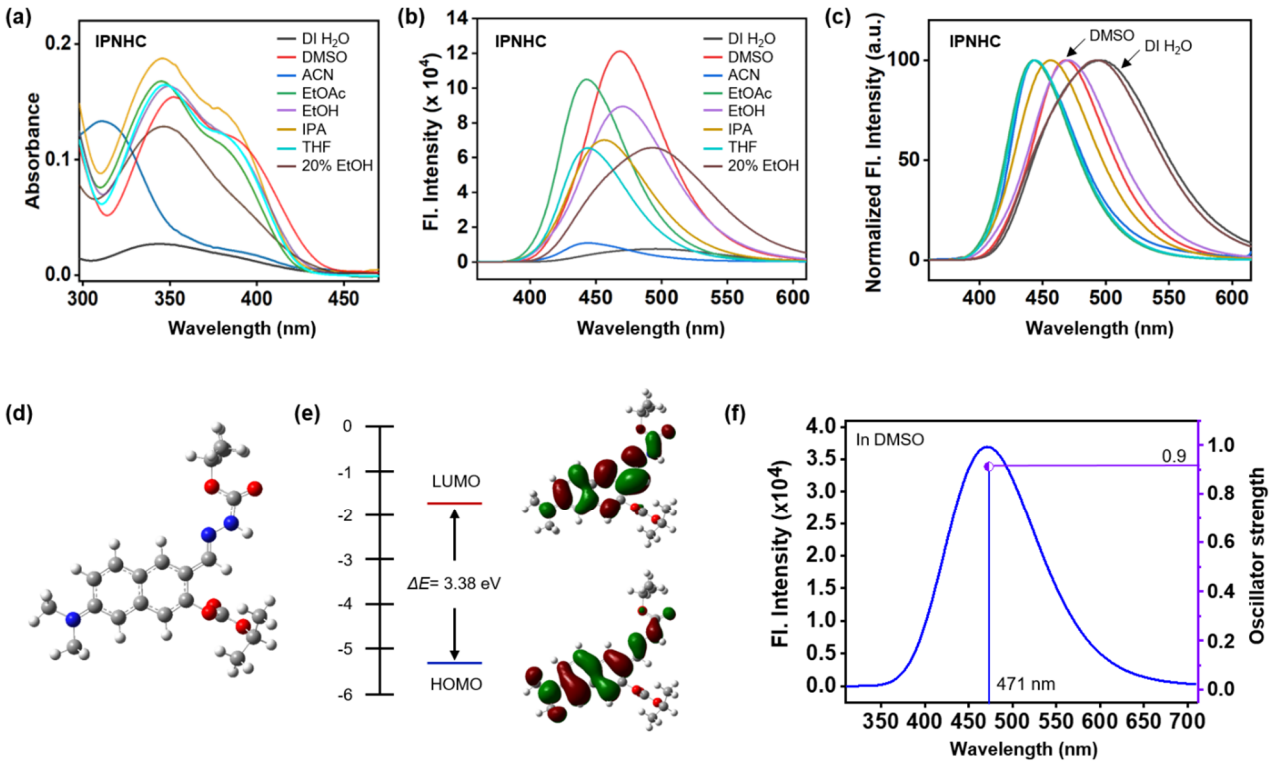

Fig. 2. Photophysical properties of IPNHC. (a) UV-visible absorption and (b) emission spectra of IPNHC (10 μM) in various solvents at 25 °C. The emission spectra were recorded upon excitation at the maximum absorption wavelength (Table S1, ESI†). (c) Normalized emission spectra of IPNHC in various solvents. (d) The optimized molecular structure and (e) HOMO/LUMO with energy levels of IPNHC by DFT calculations (B3LYP-d3/6-31+G(d) scrf=(iefpcm, solvent=DMSO). (f) Calculated S_1 emission spectrum and oscillator strength (S_1 –> S_0) of IPNHC.

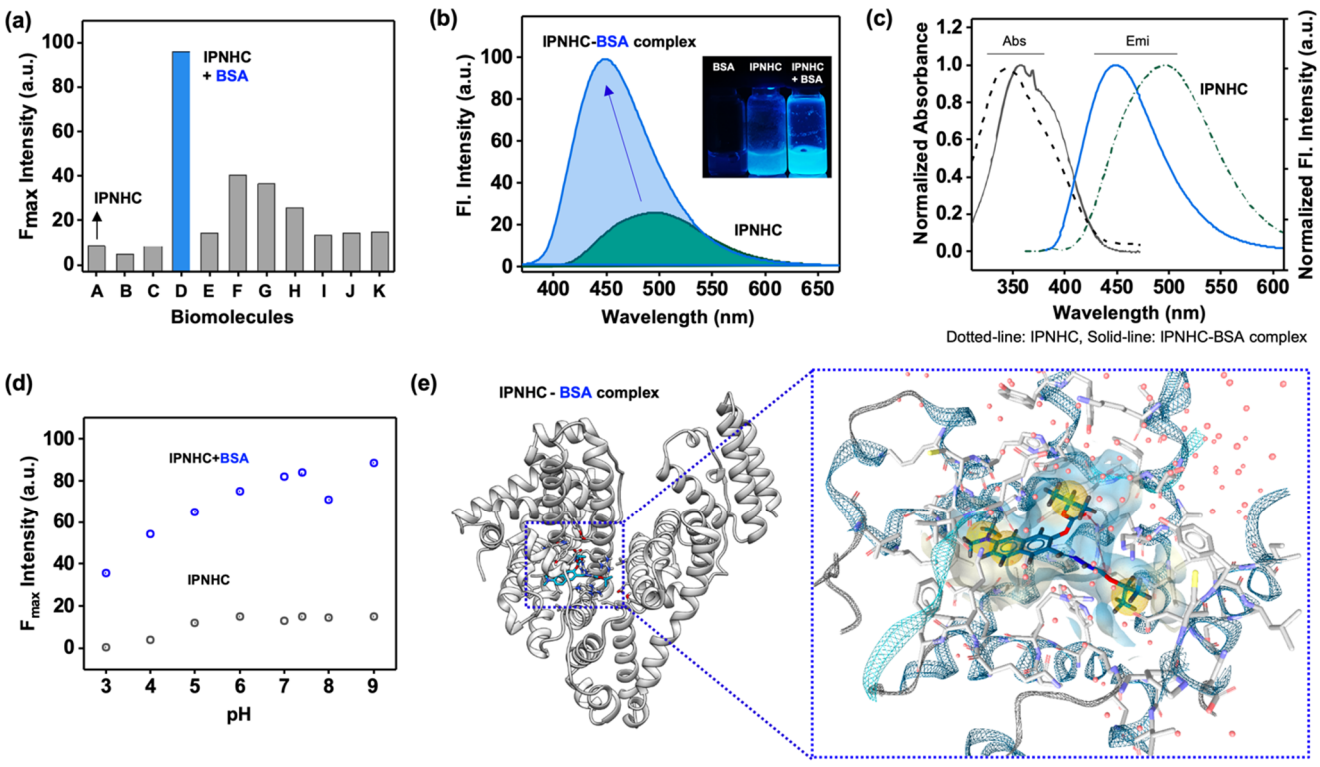

Fig. 3. Photophysical properties and molecular docking analysis of IPNHC-BSA complex. (a) Fluorescence intensity plot of IPNHC (10 μM) (peak height: 494 nm for A-C and E-K, 450 nm for D) measured 10 min after adding various biomolecules in deionized water (DI H_2O) at 25 °C. (A) IPNHC, (B) Sucrose (0.1 g/mL), (C) Homocysteine (10 mM), (D) Bovine serum albumin (50 mg/mL), (E) Glucose (10 mM), (F) Gelatin (0.2% w/v), (G) Poly-L-Lysine (0.02% w/v), (H) L-arginine (10 mM), (I) Cysteine (10 mM), (J) Glutamine (10 mM), and (K) GSH (10 mM). Excitation wavelength: 356 nm. (b) Emission spectra of IPNHC and IPNHC-BSA in the set of panels (a). Excitation wavelength: 356 nm. Inset photo: BSA, IPNHC, and IPNHC-BSA complex in DI H_2O under UV light (365 nm, power: <1 W). (c) Normalized absorption and emission spectra of IPNHC and IPNHC-BSA complex in DI H_2O. Dotted line: IPNHC, Solid-line: IPNHC-BSA complex. (d) Fluorescence intensity plot of IPNHC and IPNHC-BSA complex (peak height: 494 nm for IPNHC, 450 nm for IPNHC+BSA) within various pH buffers (pH 3–9). The emission spectra were recorded under excitation at the maximum absorption wavelength. (e) Molecular docking analysis of IPNHC and BSA. Left: INPHC (cyan) within site 1 of BSA. The protein side chains (gray) within 5Å of the docked compound are presented with the water molecules omitted for clarity. Right-box: IPNHC (cyan) in the binding pocket. Blue: nitrogen, red: oxygen, yellow: sulfur, gray: hydrogens of INPHC, and yellow ball: lipophilic interaction. Oxygens in the water molecules are represented in red dots.

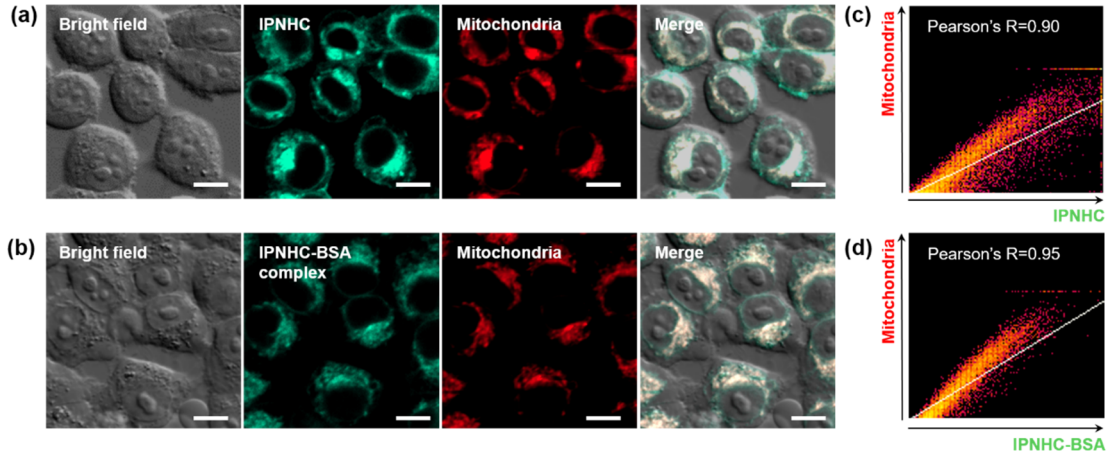

Fig. 4. CLSM images of HeLa cells with IPNHC and IPNHC-BSA complex. (a) Bright-field and CLSM images of HeLa cells treated with IPNHC (20 μM, Green) and (b) IPNHC-BSA complex (20 μM of IPNHC + 50 mg/mL of BSA), co-incubated with Mitotracker-Red (indicated as Mitochondria). Scale bar: 10 μm. Excitation wavelength and detection channel: IPNHC and IPNHC-BSA complex (Excitation: 405 nm, Detection: 405–559 nm), Mitotracker-Red (Excitation: 640 nm, Detection: 656–700 nm). (c, d) Linear fitting plot to obtain the Pearson correlation coefficient (PCC) for mitochondria. The fitting data was derived from panel (a) and (b). The PCC values (IPNHC vs. Mitochondria, IPNHC-BSA complex vs. Mitochondria) were calculated using FiJi Image-J software. Colocalization assay with the lysosome and endoplasmic reticulum (ER) are shown in Fig. S11, ESI†.

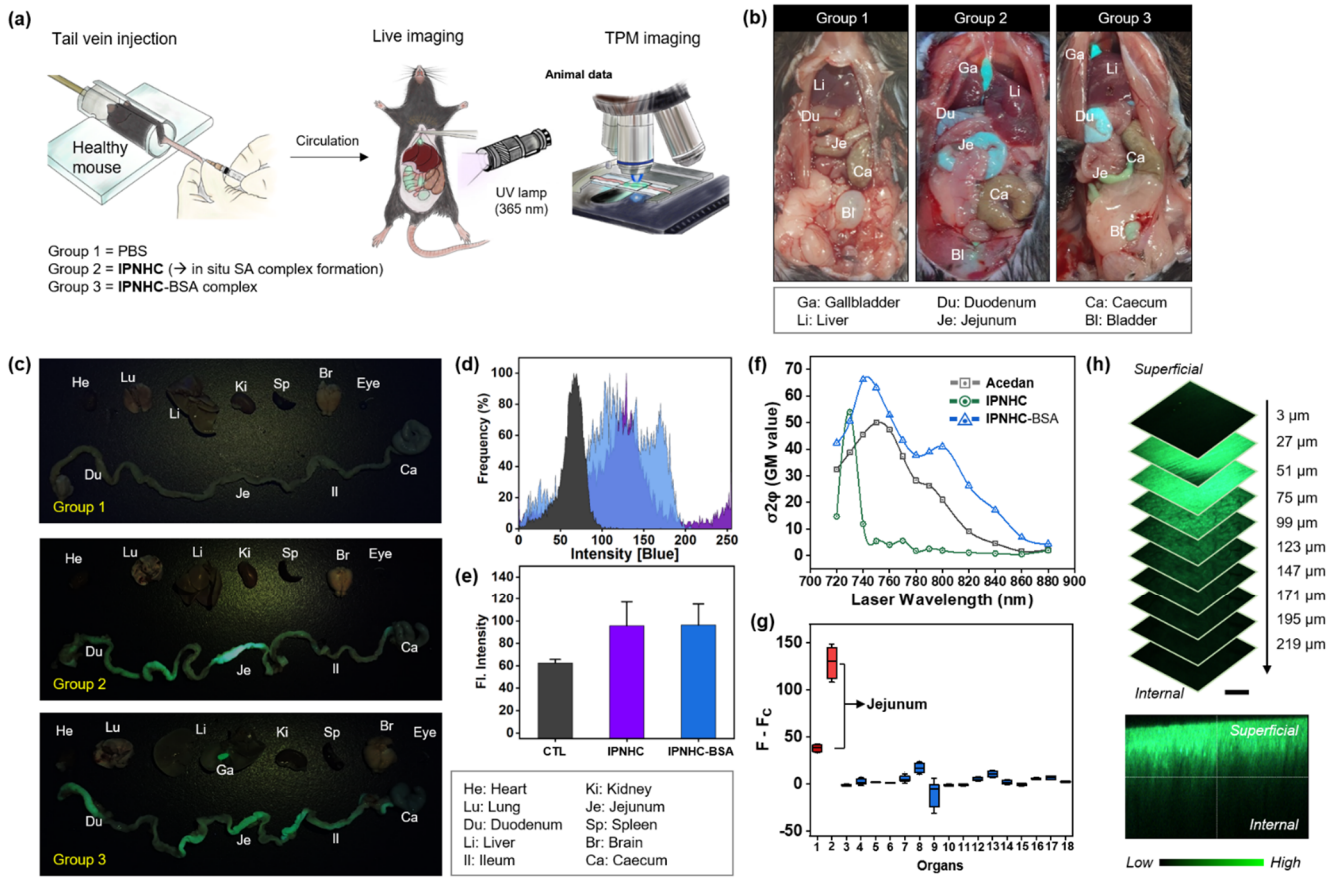

Fig. 5. In vivo and ex vivo fluorescence imaging application of mouse organs with IPNHC-BSA complex. (a) Experimental scheme of the imaging applications using the IPNHC-BSA complex. Group 1: phosphate-buffered saline (PBS, pH 7.4, 100 μL). Group 2: IPNHC (5.0 mg/kg in PBS, 100 μL). Group 3: IPNHC-BSA complex (5.0 mg/kg IPNHC in 50 mg/mL of BSA in PBS, 100 μL). Each group was injected into the tail vein (i.v.). After 30 min circulation, the abdominal region was monitored in vivo with a UV lamp (365 nm), and then the dissected organs were analyzed with two-photon microscopy (TPM). (b) In vivo fluorescence images of mouse internal organs with abdominal incision after treatment (Groups 1–3). The images were recorded at 30 min after injection. (c) Ex vivo images of dissected organs under a UV lamp (365 nm, irradiation time: <1 min, power: <1 W). All the images were taken from the same height. (d) Fluorescence histogram profiles within the intestine at the blue channel. The signal was analyzed by Image-J software (see the histogram profiles of green signal in Fig. S14, ESI†). Black area: Group 1, Purple area: Group 2, and Blue area: Group 3. (e) Average fluorescent intensity plot taken from the panel (d). Each error bar represents mean ± SD, and the values were calculated from the triplicate measurement. (f) Two-photon action cross-section (TPACS) values of IPNHC and IPNHC-BSA complex in PBS buffer (pH 7.4). (g) The two-photon intensity plot of the dissected organs in the panel (c). Odd number: IPNHC-injected group. Even number: IPNHC-BSA complex-injected group. 1&2: Jejunum, 3&4: Brain, 5&6: Colon, 7&8: Lung, 9&10: Eye, 11&12: Heart, 13&14: Kidney, 15&16: Liver, and 17&18: Spleen. The values were obtained from the Z-sum image (Fig. S16, ESI†) using FiJi Image-J software. TPM Excitation: 750 nm. Detection channel: 430–605 nm. Laser power: 50 mW at the focal plane. (h) (top) Layered TPM images of the jejunum (Group 3) following the indicated vertical depths (0–219 μm) and (bottom) its lateral resolution. Scale bar: 200 μm.

Table of Contents

Visualizing Mitochondria and Mouse Intestine with a Fluorescent Complex of Naphthalene-based Dipolar Dye and Serum Albumin

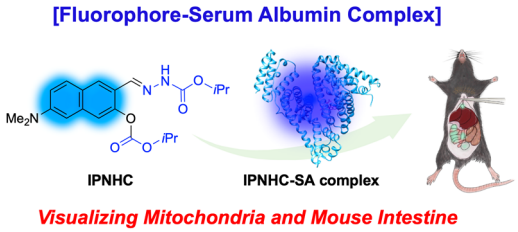

Synopsis

A fluorophore-protein complex for the visualization of mitochondria and the mouse intestine was developed for the first time. The complex formation of a newly synthesized naphthalene-based dipolar dye and serum albumin was identified, and its photophysical properties, quantum calculations, molecular docking analyses, and fluorescence imaging applications were systematically investigated.